Parameter identification of a phase-field fracture model using integrated digital image correlation

Viktor Kosin, Amélie Fau, Clément Jailin, François Hild, Thomas Wick

Parameter identification of a phase-field fracture model using integrated digital image correlation

V. Kosin[a,b,*], A. Fau[a], C. Jailin[c], F. Hild[a], T. Wick[b,a]

[a] *Université Paris-Saclay, CentraleSupélec, ENS Paris-Saclay, CNRS LMPS – Laboratoire de Mécanique Paris-Saclay, Gif-sur-Yvette, France*
[b] *Leibniz University Hannover, Institute of Applied Mathematics, Hannover, Germany*
[c] *GE HealthCare, Buc, France*

Abstract

Phase-field fracture (PFF) modeling is a popular approach to model and simulate fracture processes in solids. Accurate material parameters and boundary conditions are of utmost importance to ensure a good prediction quality of numerical simulations. In this work, an Integrated Digital Image Correlation (IDIC) algorithm is proposed to calibrate boundary conditions, Poisson's ratio, fracture energy and internal length, all at once, by using the phase-field model itself and images of a deforming sample. The presented approach is applied to virtual experiments mimicking a single edge notched shear test and implemented in the open-source `deal.II`-based software `pfm-cracks` and the digital image correlation library `Correli 3.2`. The reliability of the results is investigated for different levels of acquisition noise, thereby demonstrating high robustness and accuracy for a wide range of noise levels. The conditioning of the problem is analyzed via sensitivity fields for all parameters and the eigendecomposition of the Hessian matrix used in the IDIC algorithm.

Keywords: Phase-field fracture modeling, digital image correlation (DIC), Conditioning, Sensitivity analysis

*Corresponding author
Email addresses: `viktor.kosin@ens-paris-saclay.fr` (V. Kosin), `amelie.fau@ens-paris-saclay.fr` (A. Fau), `clement.jailin@ge.com` (C. Jailin), `francois.hild@ens-paris-saclay.fr` (F. Hild), `thomas.wick@ifam.uni-hannover.de` (T. Wick)

1. Introduction

Fracture assessment is a current topic in engineering and applied mathematics. To model fracture, various approaches are known such as boundary finite elements [13], displacement discontinuity methods [14], cohesive-zone models [88], generalized/extended finite elements [60, 22, 4], peridynamics [76] or (regularized) variational phase-field fracture models [7, 59, 47, 8]. In this work, the latter ones are of interest, namely, phase-field approaches, which share close relationships with damage models [53, 52, 72, 54, 17, 15]. Based on energy formulations of brittle fracture [21] and their numerical implementation [7], this approach has been further developed and applied in numerous situations [8, 83, 9, 18, 82]. It is intriguing because the crack path, crack direction, and crack tip velocity are obtained within the model in an implicit fashion without explicit need to compute stress intensity factors and crack front positions. Moreover, it is relatively easy to apply (except the computational cost) to two- and three-dimensional spatial settings. Further, crack initiation is included (see, for instance, L-shaped panel tests [1], where further theoretical and computational analyses about its functionality are carried out [80, 48]).

To date, in most studies, the primary focus is on so-called forward models in which the phase-field framework with given model, numerical, and material parameters is employed to compute the material state, which is theoretically, computationally, or experimentally analyzed. Here, one important goal is to use numerical simulations to predict the behavior of components within developments of new materials or work tools. Much less work has been carried in inverse modeling and optimization in which unknown parameters or boundary conditions are to be computed by comparing the numerical simulations to experimental data sets. Some recent work on optimal control with phase-field fracture shows how the phase-field model is driven into some desired states by adapting boundary conditions [64, 65, 61, 42, 43]. Topology optimization was designed [16], and stochastic phase-field modeling [24] was discussed. Parameter identification based on lower-scale simulations (*e.g.*, via molecular dynamics), which are then employed within phase-field fracture models, was proposed in Refs. [27, 71]. The closest studies in their objectives to the present one, by addressing parameter identification, are found in Refs. [44, 85, 69, 70]. However, therein Bayesian inversion [77] techniques were employed. The main novelty of the current work is to use digital image correlation

to estimate unknown parameters, and to the best of the authors' knowledge the integrated combination of images and phase-field simulations has not yet been proposed in the literature.

Phase-field models have been probed against experimentally measured kinematic fields on a qualitative basis essentially. First, simulated strain fields were compared to experimental strain fields measured via digital image correlation [66, 62, 19, 37, 87]. Similarly, displacement fields were used instead [84]. Second, crack patterns were also compared when imaged via X-ray computed tomography [66, 81] when 3D simulations were driven by measured boundary conditions. In all the aforementioned references, the internal length was not calibrated, even though it is believed to be a material parameter (see [67, 59] with more references cited therein). On the other hand, from the mathematical viewpoint the length scale was initially introduced as a regularization parameter [7] as in nonlocal damage models. The internal length was identified by using force/strain data for bone [36]. The full strain validations were performed from a purely statistical point of view (and not experimental field against simulated field).

In the context of nonlocal damage, several routes have been considered to calibrate the internal (or also called characteristic) length. It was first estimated experimentally by an energetic approach as the ratio of the fracture energy to the energy dissipated per unit volume of the material [55, 5]. An identification based on several load deflection curves from three point bending tests was proposed [49]. However, it was shown that the identification of the internal length based on such global curves did not lead to a unique solution [38]. It was suggested to calibrate a non-local damage model from discrete models [86]. An identification of the damage parameters based on digital image correlation (DIC) data was also considered [23]. The internal length was identified without coupling DIC and the identification procedure. The DIC measurements included a restricted area of the sample with a relatively small number of pixels.

In the following, it is proposed to investigate the feasibility of calibrating the internal length of a phase-field model by using displacement field measurements. This parameter is the most delicate [40]. Other material parameters will also be sought (*i.e.*, Poisson's ratio and fracture energy). To make the analysis even more challenging, the boundary conditions will also be considered unknown. Various methods exist to calibrate material parameters from full-field measurements [25]. In this study, the displacement fields

are determined via digital image correlation [79, 78]. Series of images of two synthetic tests, generated with multiple acquisition noise levels, were constructed by using simulated displacement fields. Instead of following a two-step procedure, namely, first measuring displacement fields via DIC and then post-processing them to extract the unknown parameters, integrated digital image correlation (IDIC) was selected [51, 57]. It performs registrations using mechanically admissible displacement fields (*i.e.*, the two steps are merged into a unique minimization). This approach enables, for instance, meshes to be tailored as fine as needed for numerical reasons [51, 56, 33] instead of controlled by measurement uncertainties.

The outline of this paper is as follows. In Section 2, the overall notations of this paper and integrated digital image correlation are introduced. Section 3 is devoted to the governing phase-field model used herein. Section 4 introduces the integrated computational framework applied to applications for parameter identification.

2. Integrated digital image correlation

Let $\Omega \subset \mathbb{R}^2$ be the region of interest and $\mathcal{I} := (0, T)$ be the time interval of interest, where $T > 0$ is the end time value. Moreover, let $\Omega \times \mathcal{I}$ be the so-called space-time cylinder.

2.1. Digital image correlation and space-time framework

Digital image correlation has proven to be a powerful tool to measure displacement fields [79, 35, 78]. Assuming brightness conservation, one can register an image $I_0 : \Omega \to \mathbb{R}$ with a series of images $I : \Omega \times \mathcal{I} \to \mathbb{R}$. Then, there is a displacement field $\boldsymbol{u} : \Omega \times \mathcal{I} \to \mathbb{R}^2$ such that

$$I_0(\boldsymbol{x}) = I(\boldsymbol{x} + \boldsymbol{u}(\boldsymbol{x}, t), t) =: I^{\boldsymbol{u}}(\boldsymbol{x}, t), \quad \forall (x, t) \in \Omega \times \mathcal{I}. \tag{1}$$

The underlying problem to solve is constructed by minimizing the squared differences of the reference image I_0 and the backdeformed series of images $I^{\boldsymbol{u}}$ over the space-time cylinder $\Omega \times \mathcal{I}$.

Problem 1 (DIC). *Find a displacement field* $\boldsymbol{u} \in \mathbb{V} := L^2(\mathcal{I}; L^2(\Omega))$ *such that*

$$\boldsymbol{u} = \underset{\boldsymbol{v} \in \mathbb{V}}{\arg\min}\, \mathcal{J}_1(\boldsymbol{v}), \tag{2}$$

with

$$\mathcal{J}_1(\boldsymbol{v}) := \|I^{\boldsymbol{v}} - I_0\|_{\mathbb{V}} \quad \textit{and} \quad \|\cdot\|_{\mathbb{V}}^2 := \int_{\mathcal{I}} \int_{\Omega} \cdot^2 \, \mathrm{d}x \, \mathrm{d}t. \tag{3}$$

Remark 1. *In* $\mathbb{V}$ *there are no boundary conditions prescribed for* $\boldsymbol{u}$*. We notice that this is usual in DIC since the boundary is considered in the corresponding numerical solution algorithm, and consequently the final solution is unique. A detailed discussion about the well-posedness of the static problem and the use of* $L^2(\Omega)$ *in space is given in Ref. [20].*

Remark 2. *Regular DIC algorithms are not formulated in a space-time framework, such that the displacement field is computed for each image* I_t *of the series of images* I *separately [79]. But the space-time approach has proven to be more robust with respect to noise and low sensitivities, not only for DIC but also for integrated digital image correlation (IDIC, see next sub-section), which is expected to be important for the calibration of the internal length. A more detailed discussion about the advantages of space-time formulations for DIC can be found in Ref. [6] and for IDIC in Refs. [57, 63].*

2.2. Integrated identification

IDIC is a method to identify parameters of some mechanical models directly from images [34, 51]. Based on Problem 1, one is again minimizing the squared differences between a reference image and a backdeformed series of images, but the unknown $\boldsymbol{u}$ is made explicitly dependent on the sought parameters. Let $\mathbb{P}$ be a vector space of possible parameterizations and $\mathcal{M} : \mathbb{P} \to \mathbb{V}$ be a model that computes a displacement field for the parameterization $\boldsymbol{p} \in \mathbb{P}$, then one can substitute the displacement by the model response,

$$\boldsymbol{u} = \mathcal{M}(\boldsymbol{p}). \tag{4}$$

Therefore the new problem reads as follows:

Problem 2 (IDIC)**.** *Let I_0 be a reference image, I_t a series of images and $\mathcal{M}$ a model. Find a parameterization $\boldsymbol{p} \in \mathbb{P}$ such that*

$$\boldsymbol{p} = \arg\min_{\boldsymbol{q}\in\mathbb{P}} \mathcal{J}_2(\boldsymbol{q}) \tag{5}$$

with

$$\mathcal{J}_2(\boldsymbol{q}) := \|I^{\mathcal{M}(\boldsymbol{q})} - I_0\|_{\mathbb{V}}^2. \tag{6}$$

Assuming $\mathcal{M}(\boldsymbol{p})$ to be Fréchet differentiable with derivative $\partial\mathcal{M}(\boldsymbol{p})(\boldsymbol{q})$, then a solution to Problem 2 needs to fulfill the following first-order optimality condition

$$\partial\mathcal{J}_2(\boldsymbol{p})(\boldsymbol{q}) := \int_{\mathcal{I}}\int_{\Omega} (\partial\mathcal{M}(\boldsymbol{p})(\boldsymbol{q}) \cdot \nabla I^{\mathcal{M}(\boldsymbol{p})})(I^{\mathcal{M}(\boldsymbol{p})} - I_0)\,\mathrm{d}x\,\mathrm{d}t = 0 \quad \forall \boldsymbol{q} \in \mathbb{P}. \tag{7}$$

Solving Equation (7) is a nonlinear problem, and Newton's method is proposed as the solution strategy. Assuming that $\mathcal{M}(\boldsymbol{p})$ is twice Fréchet differentiable with the second-order derivative $\partial^2\mathcal{M}(\boldsymbol{p})(\boldsymbol{\delta p}, \boldsymbol{q})$, the corresponding Hessian reads [63]

$$\begin{aligned}\partial^2\mathcal{J}_2(\boldsymbol{p})(\boldsymbol{\delta p}, \boldsymbol{q}) = \int_{\mathcal{I}}\int_{\Omega} &(\partial^2\mathcal{M}(\boldsymbol{p})(\boldsymbol{\delta p}, \boldsymbol{q}) \cdot \nabla I^{\mathcal{M}(\boldsymbol{p})})(I^{\mathcal{M}(\boldsymbol{p})} - I_0) \\ &+ (\partial\mathcal{M}(\boldsymbol{p})(\boldsymbol{\delta p}) \cdot \nabla^2 I^{\mathcal{M}(\boldsymbol{p})} \cdot \partial\mathcal{M}(\boldsymbol{p})(\boldsymbol{q}))(I^{\mathcal{M}(\boldsymbol{p})} - I_0) \\ &+ (\partial\mathcal{M}(\boldsymbol{p})(\boldsymbol{\delta p}) \cdot \nabla I^{\mathcal{M}(\boldsymbol{p})})(\partial\mathcal{M}(\boldsymbol{p})(\boldsymbol{q}) \cdot \nabla I^{\mathcal{M}(\boldsymbol{p})})\,\mathrm{d}x\,\mathrm{d}t.\end{aligned} \tag{8}$$

For the computation of both, $\partial\mathcal{M}(\boldsymbol{p})(\boldsymbol{q})$ and $\partial^2\mathcal{M}(\boldsymbol{p})(\boldsymbol{\delta p}, \boldsymbol{q})$ a finite-difference scheme is introduced. Since $\mathbb{P}$ is a vector space, there exists a basis $\{\Phi_i^p\}$ such that $\boldsymbol{q} = \sum_j a_j\Phi_j^p$ and $\boldsymbol{\delta p} = \sum_j b_j\Phi_j^p$ for any $(\boldsymbol{q}, \boldsymbol{\delta p}) \in \mathbb{P}^2$. Last, the derivatives are approximated as

$$\partial\mathcal{M}(\boldsymbol{p})(\boldsymbol{q}) \approx \sum_i \frac{\mathcal{M}(\boldsymbol{p} + s\Phi_i^p) - \mathcal{M}(\boldsymbol{p})}{s} a_i =: M_s'(\boldsymbol{p})(\boldsymbol{q}), \tag{9}$$

and

$$\partial^2\mathcal{M}(\boldsymbol{p})(\boldsymbol{\delta p},\boldsymbol{q}) \approx \sum_{i,j} \frac{\mathcal{M}(\boldsymbol{p}+s\Phi_i^p+s\Phi_j^p)-\mathcal{M}(\boldsymbol{p}+s\Phi_i^p)-\mathcal{M}(\boldsymbol{p}+s\Phi_j^p)+\mathcal{M}(\boldsymbol{p})}{s^2} a_i\, b_j =: M_s''(\boldsymbol{p})(\boldsymbol{\delta p},\boldsymbol{q}), \tag{10}$$

where $s>0$ is a given fixed perturbation parameter. Assuming that $\mathbb{P}$ is n-dimensional, with $n\in\mathbb{N}$ being a finite number, M' needs n evaluations of $\mathcal{M}$ and M'' needs n^2 evaluations of $\mathcal{M}$. In the case of the phase-field model, which is described in the next section, the computation of M'' is extremely expensive even for a low-dimensional parameter space. Since the term $\partial^2\mathcal{M}$ includes the residuals

$$\rho(\boldsymbol{x},t) := I^{\mathcal{M}(\boldsymbol{p})}(\boldsymbol{x},t) - I_0(\boldsymbol{x}), \tag{11}$$

which tend to zero near the solution, it is neglected. Together with the finite-difference approximation, the new (approximated) Jacobian reads

$$A_s(\boldsymbol{p})(\boldsymbol{q}) := \int_{\mathcal{I}}\int_{\Omega} (M_s'(\boldsymbol{p})(\boldsymbol{q})\cdot\nabla I^{\mathcal{M}(\boldsymbol{p})})(I^{\mathcal{M}(\boldsymbol{p})}-I_0)\,\mathrm{d}x\,\mathrm{d}t, \tag{12}$$

and the new (approximated) Hessian becomes

$$\begin{aligned}\partial A_s(\boldsymbol{p})(\boldsymbol{\delta p},\boldsymbol{q}) = \int_{\mathcal{I}}\int_{\Omega} &(\partial\mathcal{M}(\boldsymbol{p})(\boldsymbol{\delta p})\cdot\nabla^2 I^{\mathcal{M}(\boldsymbol{p})}\cdot\partial\mathcal{M}(\boldsymbol{p})(\boldsymbol{q}))(I^{\mathcal{M}(\boldsymbol{p})}-I_0)\\ &+(\partial\mathcal{M}(\boldsymbol{p})(\boldsymbol{\delta p})\cdot\nabla I^{\mathcal{M}(\boldsymbol{p})})(\partial\mathcal{M}(\boldsymbol{p})(\boldsymbol{q})\cdot\nabla I^{\mathcal{M}(\boldsymbol{p})})\,\mathrm{d}x\,\mathrm{d}t.\end{aligned} \tag{13}$$

The final simplified Newton algorithm for Problem 2 including line-search iterations, is given by Algorithm 1.

Algorithm 1 Newton's method for IDIC

Choose an initial guess $\boldsymbol{p}^{(0)} \in \mathbb{P}$, a basis $\{\Phi_k^{\mathbb{P}}\}$ and $s > 0$
for $i = 0, 1, 2, ...$ **do** ▷ Newton iteration
  Evaluate $\mathcal{M}(\boldsymbol{p}^i)(\Phi_k^{\mathbb{P}})$ for all k to be able to compute $M_s'(\boldsymbol{p})(\boldsymbol{q})$ for all $\boldsymbol{q} \in \mathbb{P}$
  Solve

$$\partial A_s(\boldsymbol{p}^{(i)})(\boldsymbol{\delta p}, \boldsymbol{q}) = -A_s(\boldsymbol{p}^{(i)})(\boldsymbol{q}) \quad \forall \boldsymbol{q} \in \mathbb{P} \tag{14}$$

  for $l = 0, 1, ..., l_{\max}$ **do** ▷ Line-search iteration
    $\lambda = 0.5^l$
    $\boldsymbol{p}^{(i+1)} \leftarrow \boldsymbol{p}^{(i)} + \lambda \boldsymbol{\delta p}$
    if $\mathcal{J}(\boldsymbol{p}^{(i+1)}) < \mathcal{J}(\boldsymbol{p}^{(i)})$ **then**
      Stop line-search iteration
    end if
  end for
  if $\sum_k \|\delta a_k / a_k^{(0)}\| <$ TOL with $\boldsymbol{p}^{(0)} = (a_1^{(0)}, a_2^{(0)}, ...), \boldsymbol{\delta p} = (\delta a_1, \delta a_2, ...)$, **then**
    Stop Newton iteration
  end if
end for

Remark 3. *Using again the arguments of vanishing residuals, one could also neglect the term including the Hessian matrix $\nabla^2 I^{\mathcal{M}(\boldsymbol{p})}$ in Equations (8) and (13). This simplification then results in a Gauss-Newton scheme. The vanishing residuals are achieved by good initial guesses. One can get satisfactory initial guesses by multi-level approaches using for example coarse graining or blurring of the images [35]. A more detailed discussion can be found in Refs. [74, 20].*

Remark 4. *Instead of using a finite difference scheme for the computation of $\partial \mathcal{M}(\boldsymbol{p})(\boldsymbol{q})$ and $\partial^2 \mathcal{M}(\boldsymbol{p})(\boldsymbol{\delta p}, \boldsymbol{q})$ one can also use the direct differentiation of the residual equation of the model [26].*

3. Phase-field modeling of brittle fracture

In this section, a phase-field approach is introduced to model fracture. One starts from the energy level and obtains, by differentiation, the Euler-Lagrange equations in terms of a coupled variational inequality system.

3.1. Modeling

A phase-field model based on the variational formulation of brittle fracture [21] and more precisely the related regularization form [7] is briefly introduced to specify the model $\mathcal{M}$ used in Section 4.

Assuming small displacements and linear elasticity, the infinitesimal strain tensor is written as

$$\boldsymbol{\varepsilon} := \boldsymbol{\varepsilon}(\boldsymbol{u}) = \frac{1}{2}(\boldsymbol{\nabla u} + \boldsymbol{\nabla u}^T), \tag{15}$$

and the elastic energy density function

$$\Psi_0(\boldsymbol{\varepsilon}) = \mu\, \boldsymbol{\varepsilon} : \boldsymbol{\varepsilon} + \frac{\lambda}{2}\mathrm{tr}(\boldsymbol{\varepsilon} \cdot \boldsymbol{\varepsilon}), \tag{16}$$

where μ and λ are the Lamé parameters. A smoothed scalar-valued phase-field function $\varphi : \Omega \to [0, 1]$ is introduced to model damage inside a linear elastic material. The value 0 indicates a fully damaged material, and 1 an undamaged material. Moreover, it is assumed that damage is an irreversible process (*i.e.*, no healing is possible) [52], which is modeled by $\partial_t \varphi \leq 0$ and known as the crack irreversibility constraint (i.e., an inequality constraint in time). To circumvent unrealistic damage patterns, an additive decomposition of the energy density is introduced [59, 58] with a comparison to other models made in [1]. Let $\boldsymbol{\varepsilon}(\boldsymbol{u}) = \sum_i \epsilon_i \boldsymbol{n}_i \otimes \boldsymbol{n}_i$ be the spectral decomposition of the strain tensor and $\boldsymbol{\varepsilon}_\pm(\boldsymbol{u}) := \sum_i \langle \epsilon_i \rangle_\pm \boldsymbol{n}_i \otimes \boldsymbol{n}_i$ with $\langle \cdot \rangle_\pm := \frac{1}{2}(\cdot \pm |\cdot|)$. Then, the energy density is decomposed as

$$\Psi_0(\boldsymbol{\varepsilon}) = \Psi^+(\boldsymbol{\varepsilon}) + \Psi^-(\boldsymbol{\varepsilon}), \tag{17}$$

where

$$\Psi^+(\boldsymbol{\varepsilon}) := \mu\, \boldsymbol{\varepsilon}_+ : \boldsymbol{\varepsilon}_+ + \frac{\lambda}{2}\langle \mathrm{tr}(\boldsymbol{\varepsilon}) \rangle_+^2 \quad \text{and} \quad \Psi^-(\boldsymbol{\varepsilon}) := \mu\, \boldsymbol{\varepsilon}_- : \boldsymbol{\varepsilon}_- + \frac{\lambda}{2}\langle \mathrm{tr}(\boldsymbol{\varepsilon}) \rangle_-^2 \tag{18}$$

are the extensional and contractional energy densities, respectively. Then, the regularized problem is formulated as follows: Find $\boldsymbol{u}$ and φ for almost all times t such that

$$(\boldsymbol{u}, \varphi) = \underset{(\boldsymbol{v}, \psi)}{\arg\min}\, E_\ell((\boldsymbol{v}, \psi)) \quad \text{and} \quad \partial_t \varphi \leq 0, \tag{19}$$

with

$$E_\ell((\boldsymbol{u},\varphi)) := \frac{1}{2}\int_\Omega \left((1-\kappa)\varphi^2+\kappa\right)\Psi^+(\boldsymbol{\varepsilon}(u)) + \Psi^-(\boldsymbol{\varepsilon}(u)) + G_c\left(\frac{1}{2\ell}(1-\varphi)^2 + \frac{\ell}{2}|\nabla\varphi|^2\right)\,\mathrm{d}x, \tag{20}$$

where G_c is the fracture energy, ℓ the internal length, and κ a positive regularization parameter to counteract numerical issues (zero entries on the diagonal where $\varphi = 0$ in the discrete system matrix resulting into a singular, non-solvable, linear equation system) when φ tends to 0. Since one works here in a quasi-static regime without time derivatives in the governing equations, the time-continuous crack irreversibility constraint is written in incremental form using a difference-quotient approximation

$$\partial_t\varphi \approx \frac{\varphi(t_n)-\varphi(t_{n-1})}{t_n - t_{n-1}} \tag{21}$$

with $t_n, t_{n-1} \in \mathcal{I}$. Consequently, the phase-field variable is from the following closed convex set

$$\mathbb{Y}_{in} := \{\varphi^n \in H^1(\Omega) |\ 0 \leq \varphi^n \leq \varphi^{n-1} \leq 1 \text{ a.e. in } \Omega\}.$$

The solutions $u(t_n)$ and $\varphi(t_n)$ at the time t_n are from now on denoted by u^n and φ^n. For the displacements, one uses the function space

$$\mathbb{X} := \{u \in H^1(\Omega) |\ u = u_D \text{ on } \Gamma \subset \partial\Omega\}.$$

Remark 5. *The Dirichlet boundary conditions u_D are part of the unknowns in Section 4 and are going to be computed via IDIC.*

The resulting optimization problem is then summarized as follows:

Problem 3. *Given φ^0 and for the incremental steps t_n, with $n = 1, ..., N$, find $\boldsymbol{u}^n \in \mathbb{X}$ and $\varphi^n \in \mathbb{Y}_{in}$, such that*

$$(\boldsymbol{u}^n, \varphi^n) = \underset{(\boldsymbol{v},\psi)\in\mathbb{X}\times\mathbb{Y}_{in}}{\arg\min}\ E_\ell((\boldsymbol{v},\psi)) \tag{22}$$

where E_ℓ is defined in Equation (20).

The corresponding optimality condition is given by [82][Proposition 19]

$$\partial E_\ell((\boldsymbol{u}^n,\varphi^n))((\boldsymbol{v},\psi-\varphi^n)) \geq 0 \qquad \forall (\boldsymbol{v},\psi)\in \mathbb{X}\times\mathbb{Y}_{in}, \tag{23}$$

where

$$\begin{aligned}\partial E_\ell((\boldsymbol{u},\varphi))((\boldsymbol{v},\psi)) = \int_\Omega &\left((1-\kappa)\varphi^2+\kappa\right)\partial\Psi^+(\boldsymbol{\varepsilon}(\boldsymbol{u}))(\boldsymbol{\varepsilon}(\boldsymbol{v})) + \partial\Psi^-(\boldsymbol{\varepsilon}(\boldsymbol{u}))(\boldsymbol{\varepsilon}(\boldsymbol{v}))\\ &+ (1-\kappa)\varphi\psi\,\Psi^+(\boldsymbol{\varepsilon}(\boldsymbol{u})) + G_c\left(-\frac{1}{\ell}(1-\varphi)\psi + \ell\nabla\varphi\cdot\nabla\psi\right)\mathrm{d}x\end{aligned} \tag{24}$$

and

$$\begin{aligned}\partial\Psi^+(\boldsymbol{\varepsilon}(\boldsymbol{u}))(\boldsymbol{\varepsilon}(\boldsymbol{v})) &= \mu\,\boldsymbol{\varepsilon}_+(\boldsymbol{u}):\boldsymbol{\varepsilon}(\boldsymbol{v}) + \frac{\lambda}{2}\langle\mathrm{tr}(\boldsymbol{\varepsilon}(\boldsymbol{u}))\rangle_+\mathrm{tr}(\boldsymbol{\varepsilon}(\boldsymbol{v})),\\ \partial\Psi^-(\boldsymbol{\varepsilon}(\boldsymbol{u}))(\boldsymbol{\varepsilon}(\boldsymbol{v})) &= \mu\,\boldsymbol{\varepsilon}_-(\boldsymbol{u}):\boldsymbol{\varepsilon}(\boldsymbol{v}) + \frac{\lambda}{2}\langle\mathrm{tr}(\boldsymbol{\varepsilon}(\boldsymbol{u}))\rangle_-\mathrm{tr}(\boldsymbol{\varepsilon}(\boldsymbol{v})).\end{aligned} \tag{25}$$

Unfortunately, the energy functional $E_\ell((\boldsymbol{u},\varphi))$, as defined in Equation (20), is not convex simultaneously in each variable such that the numerical solution of the fully monolithic problem becomes difficult. As proposed in Ref. [28], the solution variable in the term $\left((1-\kappa)\varphi^2+\kappa\right)\partial\Psi_+(\boldsymbol{\varepsilon}(\boldsymbol{u}))(\boldsymbol{\varepsilon}(\boldsymbol{v}))$ is approximated by a linear extrapolation in time

$$\varphi \approx \widetilde{\varphi}(\varphi^{n-1},\varphi^{n-2}) := \varphi^{n-2} + \frac{t-t^{n-2}}{t^{n-1}-t^{n-2}}(\varphi^{n-1}-\varphi^{n-2}), \tag{26}$$

where φ^{n-1} and φ^{n-2} denote the solutions at the previous times t^{n-1} and t^{n-2}, respectively. In order to still have a monolithically-coupled variational formulation, φ is not approximated in the energy functional (20), but in the optimality condition (23), such that ∂E_ℓ is approximated by the semilinear form

$$\begin{aligned}B_\ell((\boldsymbol{u},\varphi))((\boldsymbol{v},\psi)) := \int_\Omega &\left((1-\kappa)\widetilde{\varphi}^2+\kappa\right)\partial\Psi^+(\boldsymbol{\varepsilon}(\boldsymbol{u}))(\boldsymbol{\varepsilon}(\boldsymbol{v})) + \partial\Psi^-(\boldsymbol{\varepsilon}(\boldsymbol{u}))(\boldsymbol{\varepsilon}(\boldsymbol{v}))\\ &+ (1-\kappa)\varphi\psi\,\Psi_+(\boldsymbol{\varepsilon}(\boldsymbol{u})) + G_c\left(-\frac{1}{\ell}(1-\varphi)\psi + \ell\nabla\varphi\cdot\nabla\psi\right)\mathrm{d}x\end{aligned} \tag{27}$$

and the new optimality condition reads

$$\partial B_\ell((\boldsymbol{u}^n,\varphi^n))((\boldsymbol{v},\psi-\varphi^n)) \geq 0 \qquad \forall (\boldsymbol{v},\psi)\in \mathbb{X}\times\mathbb{Y}_{in}. \tag{28}$$

Equation (28) is solved by Newton's method. A detailed discussion about the solution algorithm including the derivation and computation of the Jacobian can be found in Ref. [41][Section 3].

3.2. Discretization

As a next step the solution of the phase-field model, described in the previous section, should be inserted into Algorithm 1. Therefore, a finite-element discretization, defined on a quadrilateral discretization $\mathcal{T}_h$ of Ω with elements E of size h and piecewise bilinear functions $\mathcal{Q}_1 := \text{span}\{1, x_1, x_2, x_1x_2\}$ is introduced

$$\begin{aligned} \mathbb{X}_h &:= \{\boldsymbol{v}_h \in C(\Omega) \cap \mathbb{X} : \boldsymbol{v}_h|_E \in \mathcal{Q}_1 \text{ for all } E \in \mathcal{T}_h\}, \\ \mathbb{Y}_{in,h} &:= \{\psi_h \in C(\Omega) \cap \mathbb{Y}_{in} : \psi_h|_E \in \mathcal{Q}_1 \text{ for all } E \in \mathcal{T}_h\}. \end{aligned} \tag{29}$$

The discrete optimization problem reads as follows:

Problem 4. *Given φ_h^0 and for the incremental steps t_n, with $n = 1, ..., N$, find $\boldsymbol{u}_h^n \in \mathbb{X}$ and $\varphi^n \in \mathbb{Y}_{in}$, such that*

$$(\boldsymbol{u}_h^n, \varphi_h^n) = \underset{(\boldsymbol{v}_h, \psi_h) \in \mathbb{X}_h \times \mathbb{Y}_{in,h}}{\arg\min} B_\ell((\boldsymbol{v}_h, \psi_h)), \tag{30}$$

where B_ℓ is defined in Equation (28).

3.3. Numerical solution and software

The previous system requires linear and nonlinear solvers. There exist three types of nonlinearities, (i) the variational inequality constraint due to the crack irreversibility condition, (ii) the decomposition of the strain energy, and (iii) the nonlinear coupling between the displacement equation and the phase-field variational inequality. In Ref. [28], a combined Newton algorithm was suggested in which the crack irreversibility is addressed in terms of a primal-dual active-set method and the nonlinear system with a classical line-search assisted Newton method. Both steps are combined into one loop and implemented in open-source `pfm-cracks` [30] based on the finite-element library `deal.II` [2, 3]. Recently, improvements of the combined active set and Newton solver have been suggested including supporting numerical tests [45]. Within the nonlinear combined Newton iterations, the linear systems are solved with GMRES (generalized

minimal residual method) [75], which is preconditioned with a block-diagonal system, where the blocks are approximated with algebraic multigrid from Trilinos [31]. Parallelization is based on MPI, where the adaptive meshes are organized by p4est [10].

4. Application

The previous developments are taken to design an integrated digital image correlation scheme based on the phase-field fracture model. Algorithm 1 has been implemented in the `Correli 3.2` framework, which is an extension of the 3.0 version [50], namely, a `Matlab` based library with C++ kernels for digital image correlation. The phase-field codes to determine fracture propagation are described and referenced in Section 3.3.

4.1. Small-sample experiment

The first synthetic experiment to analyze the proposed IDIC approach is a slightly adapted version of the single edge notched shear test presented in Ref. [59]. The sample is of square shape and each edge is 1 mm long, see Figure 1(a). To generate synthetic images, the phase-field model is used to compute displacement fields for time steps $t_k = k \cdot 10^{-4}$ second with $k = 0, ..., 75$. The displacement fields are then applied to the reference image shown in Figure 1(b),

$$I_t(\boldsymbol{x}, t_k) = I_0(\boldsymbol{x} - \boldsymbol{u}(\boldsymbol{x}, t_k)). \tag{31}$$

The definition (*i.e.*, number of pixels) of the deformed images is identical to that of the reference picture. Therefore Equation (31) is solved for all pixels of each synthetically deformed image. The field of view of the images is slightly larger than the sample to have the fully deformed domain inside of the images. In the reference image, the sample is identified by the speckle pattern and the added field of view by the black background. The speckle pattern was generated using a Halton sequence placing ellipses of normally distributed intensity with radii uniformly ranging from 5 to 25 px on the sample surface. The pixel size is about 1 µm.

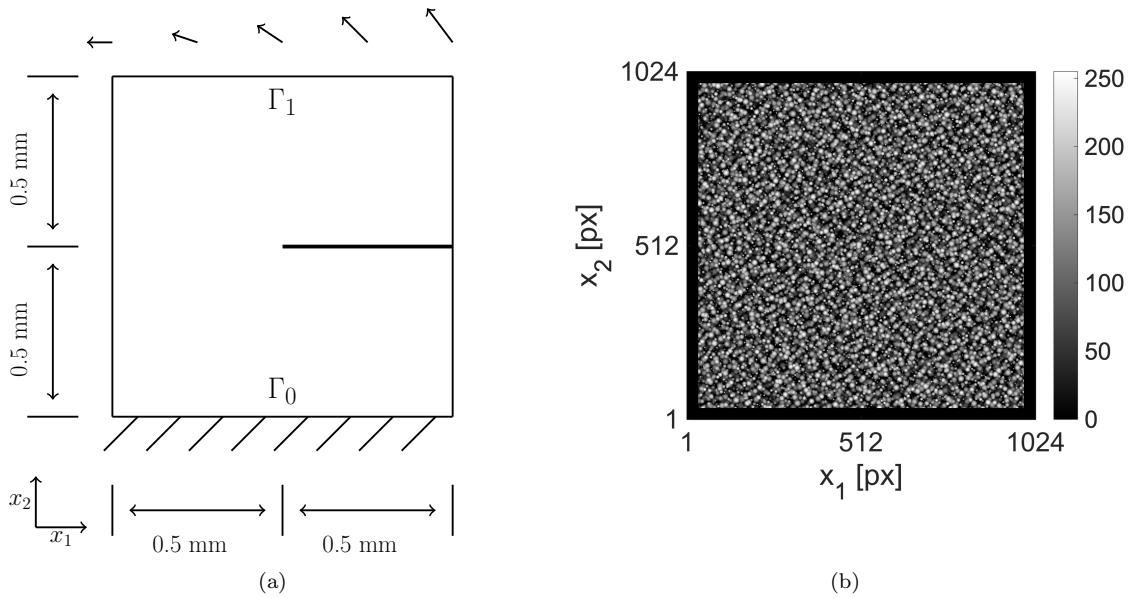

(a) (b)

Figure 1: Small-sample experiment. Geometry of the sample and applied boundary conditions (a), speckle pattern applied to the sample surface (b). The pixel size is about 1 µm.

The Dirichlet boundary conditions, chosen to be feasible using multi-axial testing machines [12], are

$$\boldsymbol{u}|_{\Gamma_0} = 0 \text{ [mm]} \quad \text{and} \quad \boldsymbol{u}|_{\Gamma_1} = (-2\,\tau, 1.5\,x_1\,\tau)^T \text{ [mm]}, \tag{32}$$

where τ is the dimensionless time. Due to the end time of $7.5 \cdot 10^{-3}$ second and a pixel size of about 1 µm, the maximum displacement at the boundary Γ_1 is going to be about 15 px The material and numerical parameters of the synthetic test are gathered in Table 1. The element size h of the structured mesh is of the order of 12 µm (or 11 px) and the internal length ℓ is assumed to be equal to 2 times the element size.

Table 1: Reference material and numerical parameters to generate the displacement fields for the deformed configurations for the small-sample experiment.

Parameter	Definition	Value
h	Diagonal cell diameter	12 µm (or $\approx$ 11 px)
G_c	Fracture energy	2.7 kJ/m^2
E	Young's modulus	250 GPa
ν	Poisson's ratio	0.2
ℓ	Internal length	$2\,h \approx 24$ µm (or $\approx$ 22 px)
κ	Regularization parameter	10^{-10}

The resulting displacement field together with the phase-field solution at frame 75 are shown in Figure 2.

The crack starts propagating from the beginning of the slit at frame 43 toward the bottom/left corner.

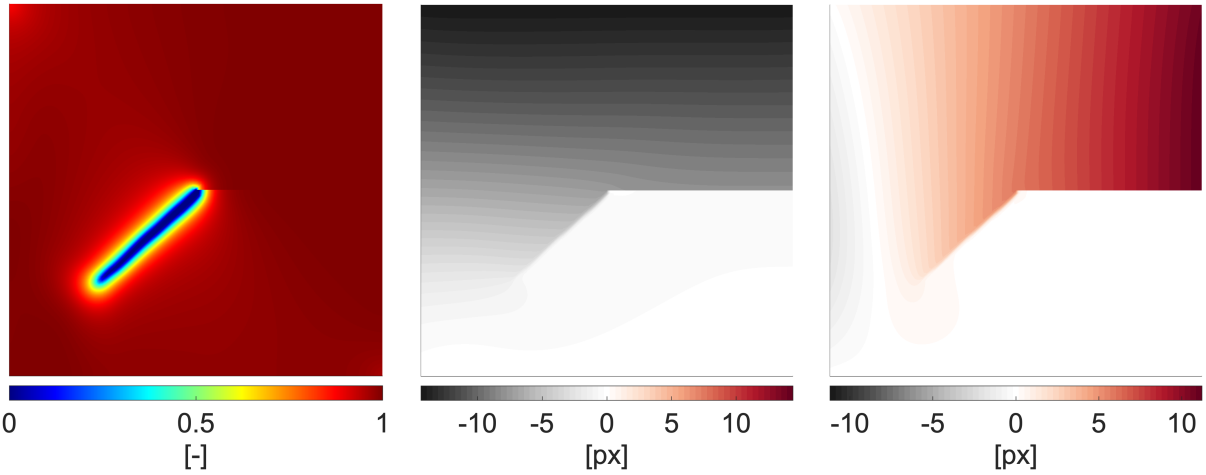

Figure 2: Solution of the phase-field model of the small-sample test at frame 75 for the reference parameters. Phase-field variable φ (a), displacements u_1 (b) and u_2 (c).

In practice, one typically performs a first measurement using standard DIC techniques to estimate the boundary conditions, and take them as known for IDIC analyses [57], such that only material parameters need to be optimized. However, numerical models are very sensitive to boundary conditions [73] with specific examples related to the current work in [12, 29], such that slightly incorrect boundary conditions (due to measurement uncertainties in DIC analyses) may influence the quality of IDIC results. Therefore, the boundary conditions as well as the material parameters are optimized simultaneously, such that the space of parameterization is chosen to be $\mathbb{P} = \mathbb{R}^5$ with two parameters controlling the boundary condition on Γ_1 and the other three parameters are the Poisson's ratio ν, the fracture energy G_c and the internal length ℓ. More precisely, a parameterization $\boldsymbol{p} = (a_1, ..., a_5)^T \in \mathbb{P}$ is defined as

$$\boldsymbol{u}(\boldsymbol{x}, t)|_{\Gamma_1 \times \mathcal{I}} = (a_1\, t, a_2\, x_1\, t)^T \text{ [mm]}, \quad \nu = a_3, \quad G_c = a_4 \quad \text{and} \quad \ell = a_5\, h, \tag{33}$$

where $\boldsymbol{x} = (x_1, x_2) \in \Gamma_1$ and $t \in \mathcal{I}$. Using this parameterization, one should be aware that the Poisson's ratio should belong to the interval $(-1, 0.5)$, and the fracture energy should be greater than zero. Furthermore, the internal length ℓ has to be at least as large as the size of one element, e.g. h such that $\ell > h$, which is a

well-known numerical requirement in the case of low-order finite elements [7][Section 2.1.2] or [82][Section 5.5]. With respect to the selected resolution, the internal length has to be larger than 11 px. Consequently, one has to add inequality constraints

$$-1 < a_3 < 0.5, \quad a_4 > 0 \quad \text{and} \quad a_5 \geq h, \tag{34}$$

into the minimization problem. In the presented study, a simple active-set scheme was added inside Algorithm 1. The initial parameterization

$$\boldsymbol{p}^0 = (a_1^{(0)}, ..., a_5^{(0)}) = (-1, 0.5, 0.4, 2, 3)^T \tag{35}$$

was selected because the corresponding solution did not include a crack, see Figure 3, and is therefore suitable to test the method for non-optimal initialization.

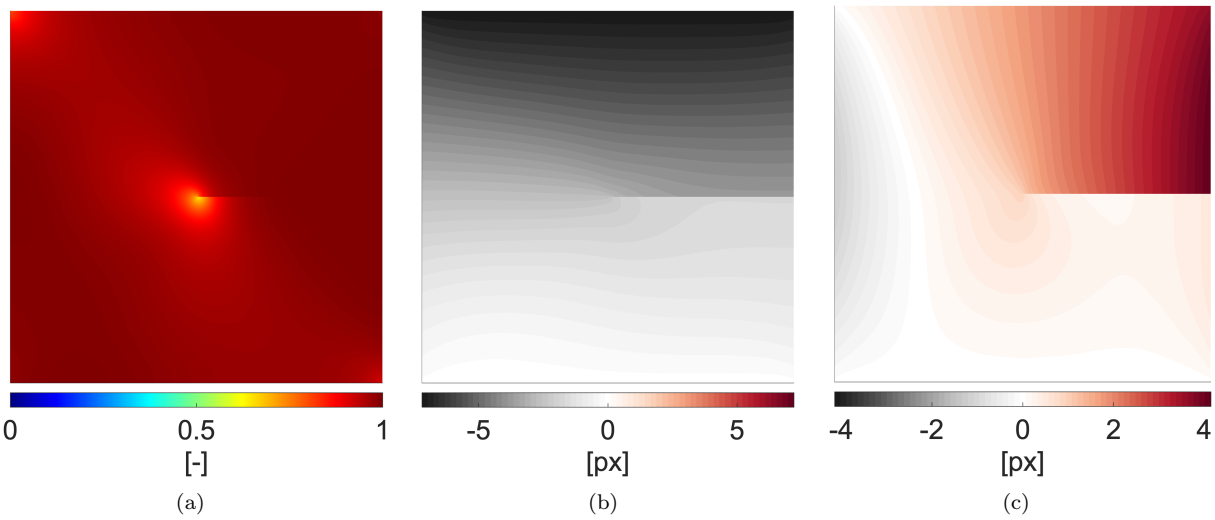

(a) (b) (c)

Figure 3: Solution of the phase-field model of the small-sample test at frame 75 for the initial parameterization $\boldsymbol{p}^{(0)}$. Phase-field variable φ (a), displacements u_1 (b) and u_2 (c).

This initial guess is also used to define the basis of $\mathbb{P}$

$$\Phi_i^{\mathbb{P}} = a_i^{(0)} \boldsymbol{e}_i, \tag{36}$$

where $\boldsymbol{e}_i$ is one in its i-th component and zero else. This definition is especially useful for the finite-difference scheme. By choosing a perturbation parameter $s = 0.01$, one automatically perturbs the parameters by 1% wrt. its initial values. As one can assume that the initial parameterization is at least of the same order as the real solution, the finite-difference approximation is a reasonably good approximation of the actual derivative of the model.

4.1.1. Sensitivity and conditioning study

The sensitivity fields $S_i = M_s'(\boldsymbol{p})(\Phi_i^{\mathbb{P}})$, where M_s' is defined in Equation (9), visually represent at which rate the displacement field changes for a given perturbation of the parameters $\boldsymbol{p}$ at a certain time instant and location. Figure 4 shows the sensitivity fields for each considered parameter at time $\tau = T$ of the converged solution, scaled by the perturbation factor $s = 0.01$. Due to the scaling, one can also interpret the sensitivity fields as the absolute variation of the displacement (in pixels) by a perturbation of 1% of the parameters $\boldsymbol{p}$. The high values of the other fields mostly concentrate around the damaged zone, while the fields of the boundary condition are very sensitive over large regions around the damaged zone and the boundary itself. The damage model parameters G_c and ℓ are sensitive in relatively large areas around the crack, even though the sensitivity values are relatively low. Despite the fact that the sensitivity fields of the phase-field variable are not directly of importance for the IDIC algorithm itself, they are indirectly part of the variation and sensitivity of the displacement field and are therefore also displayed in Figure 4. Again, the sensitivity field is scaled by the perturbation factor and therefore corresponds to the absolute variation of 1% of the parameters $\boldsymbol{p}$. Contrary to the variation of the displacement fields, the sensitivity fields of the phase-field variable clearly concentrate around the active zone of damage growth and not along the full path. Only the sensitivity field of the internal length is visible along the damage path, but the levels are much lower than for all other parameters.

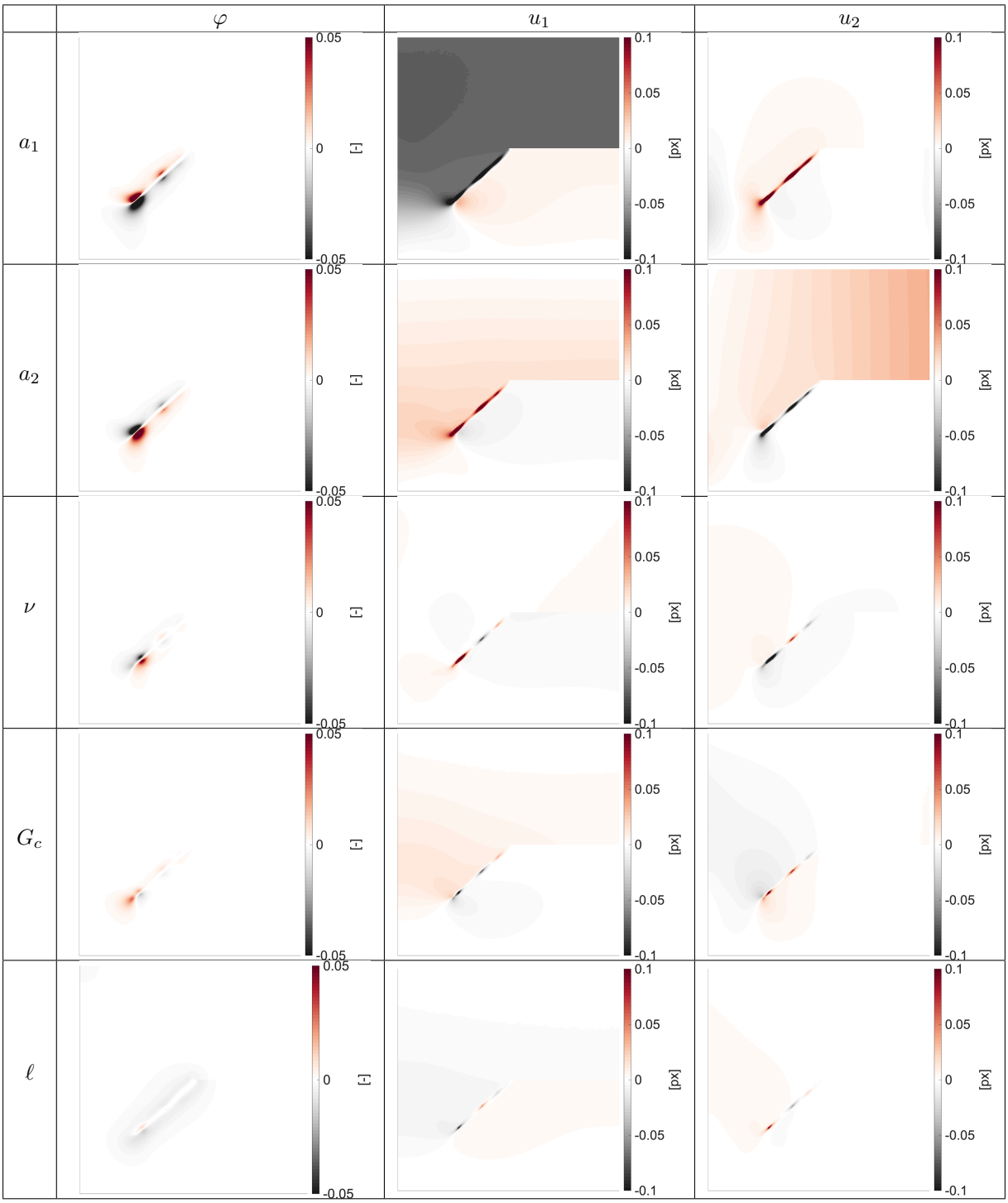

Figure 4: Variation of the phase-field variable for 1% perturbation of the parameters (left column), the first component of the displacement field (middle column) and the second component of the displacement field (right column) for the small-sample experiment. All fields are scaled by the perturbation factor $s = 0.01$.

The sensitivities can be further understood by analyzing the normalized, instantaneous IDIC Hessian

matrices

$$H_{ij}^{\text{inst}}(t) = \frac{1}{|\Omega|}\int_{\Omega}(S_i \cdot \nabla I^{\mathcal{M}(\boldsymbol{p})})(S_j \cdot \nabla I^{\mathcal{M}(\boldsymbol{p})})\,\mathrm{d}x, \tag{37}$$

and the full space-time Hessian matrix

$$H_{ij}^{\text{full}} = \frac{1}{|\Omega \times \mathcal{I}|}\int_{\mathcal{I}}\int_{\Omega}(S_i \cdot \nabla I^{\mathcal{M}(\boldsymbol{p})})(S_j \cdot \nabla I^{\mathcal{M}(\boldsymbol{p})})\,\mathrm{d}x\,\mathrm{d}t. \tag{38}$$

For both cases, the Hessian matrix of the exact solution is analyzed such that not only the first but also the second term of the true IDIC Hessian (8) were omitted. In the following, the condition numbers for the Hessian matrices are analyzed in more detail. While the condition number indicates good or bad convergence rates [68], one can also interpret it as an amplification factor of errors existing due to, *e.g.*, acquisition noise [32, 57]. The condition number of the instantaneous Hessian matrix decreases significantly with time (Figure 5) and reaches its lowest level after the damaged zone already propagated and at the end of the test. Interestingly, the condition number also increased during damage propagation. The full space-time Hessian has a lower condition number than any instantaneous Hessian.

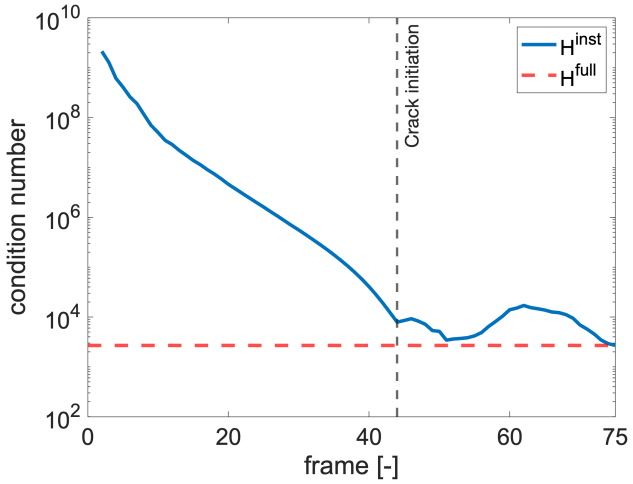

Figure 5: Condition number of the space-time Hessian matrix H^{full} compared to that of the instantaneous Hessian matrix H^{inst} for each image of the small-sample experiment.

To get a better understanding of the conditioning of the Hessian matrices, the eigendecomposition of the instantaneous Hessians is reported in Figure 6 for frames 20, 50 and 75 as well as the full space-time

Hessian. The parameters of the boundary conditions, a_1 and a_2, represent the first two eigenparameters with the highest eigenvalues for all frames. The Poisson's ratio only fully uncouples from all other parameters during the elastic deformation process such as at frame 20. Even though the Poisson's ratio remains mostly uncoupled up to frame 50, a weak coupling with respect to the fracture energy becomes visible and further, the corresponding mode becomes less sensitive than the mode of the fracture energy. Conversely, G_c and ℓ are fully coupled and the corresponding eigenparameters have very low eigenvalues. This is due to the fact that damage starts to develop in the vicinity of the slit root. The moment the damaged zone starts to propagate, the eigenparameters related to G_c and ℓ have much higher eigenvalues such that the parameter G_c becomes more sensitive than ν at frame 50. For frame 75, all eigenvalues increase and especially the eigenvalue mostly related to G_c, such that G_c and ν have almost the same sensitivity. The full space-time Hessian has the same eigenparameters as the instantaneous Hessian at frame 50, but the eigenvalues are closer to those of the instantaneous Hessian at frame 75.

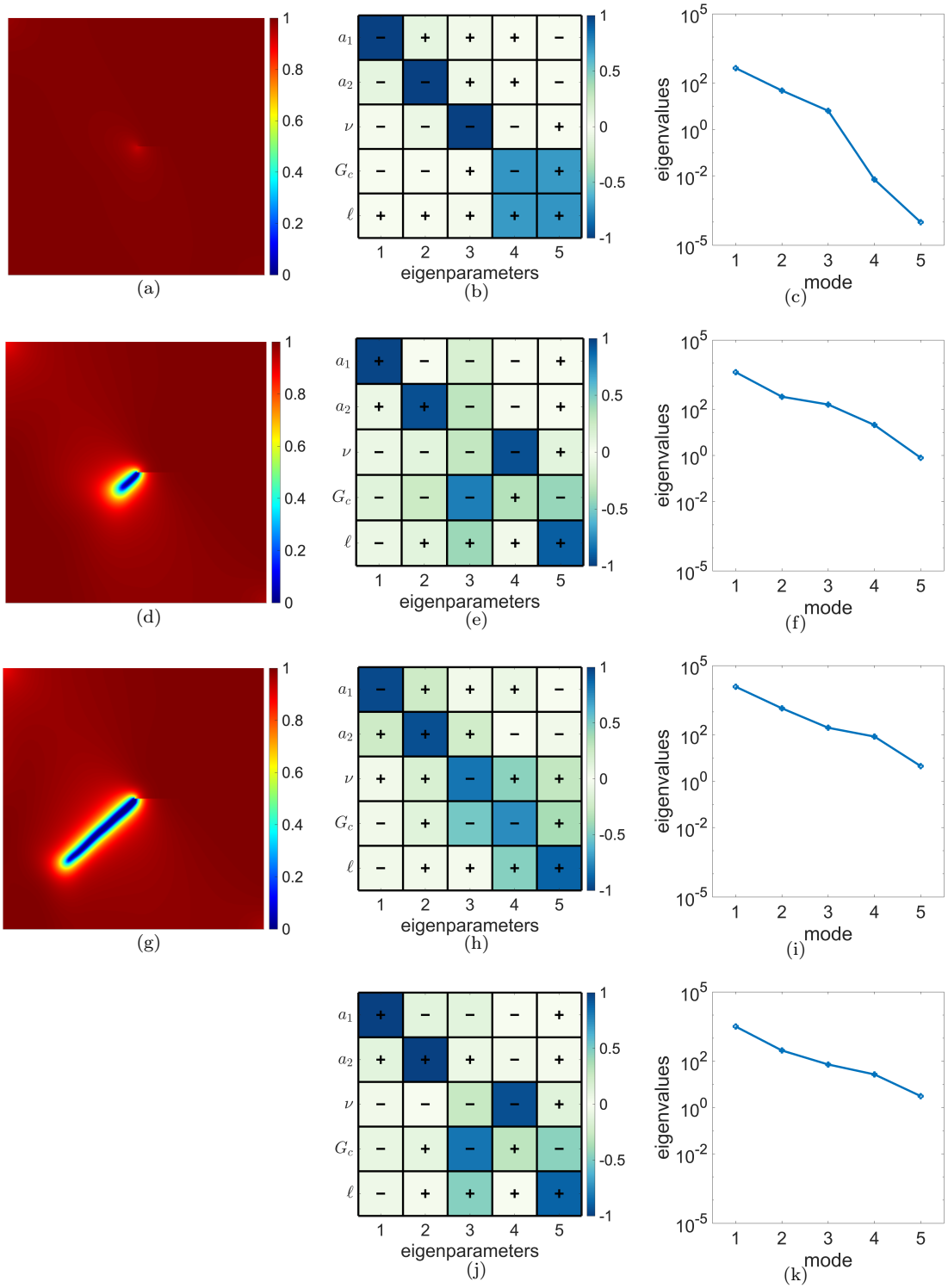

Figure 6: Solution of the phase-field variable for frames 20 (a), 50 (d) and 75 (g) for the small-sample experiment. Rows one to three correspond to instantaneous Hessian matrices and row four with the full space-time Hessian matrix. The eigendecomposition of the Hessian matrices gives the eigenparameters shown in (b,e,h,j) and the eigenvalues shown in (c,f,i,k).

4.1.2. Results

Instead of using the full sample $\Omega = [0, 10]^2$ for the IDIC problem, a slightly smaller region excluding the slit was used. At the slit, high interpolation errors were observed, which influenced the accuracy of the converged solution. The mask shown in Figure 7 corresponds to the black area. The residuals of the initial and converged parameterizations are displayed in the region of interest at frames $20, 43$ and 75, corresponding to the (essentially) elastic phase, the onset of damage propagation and the end of the test, respectively. The residuals do not vanish completely, but their RMS level is reduced from 38.7 to 1.5, and they have a periodic pattern, which is traced back to gray level (spline) interpolation errors when creating the image series $I^{\mathcal{M}(\boldsymbol{p})}$. Interestingly, the maximum value of the residuals decreases in time, as indicated by the residuals in Figure 7(d-f). This is the result of the increasing sensitivity of the parameters, which was observed in Section 4.1.1.

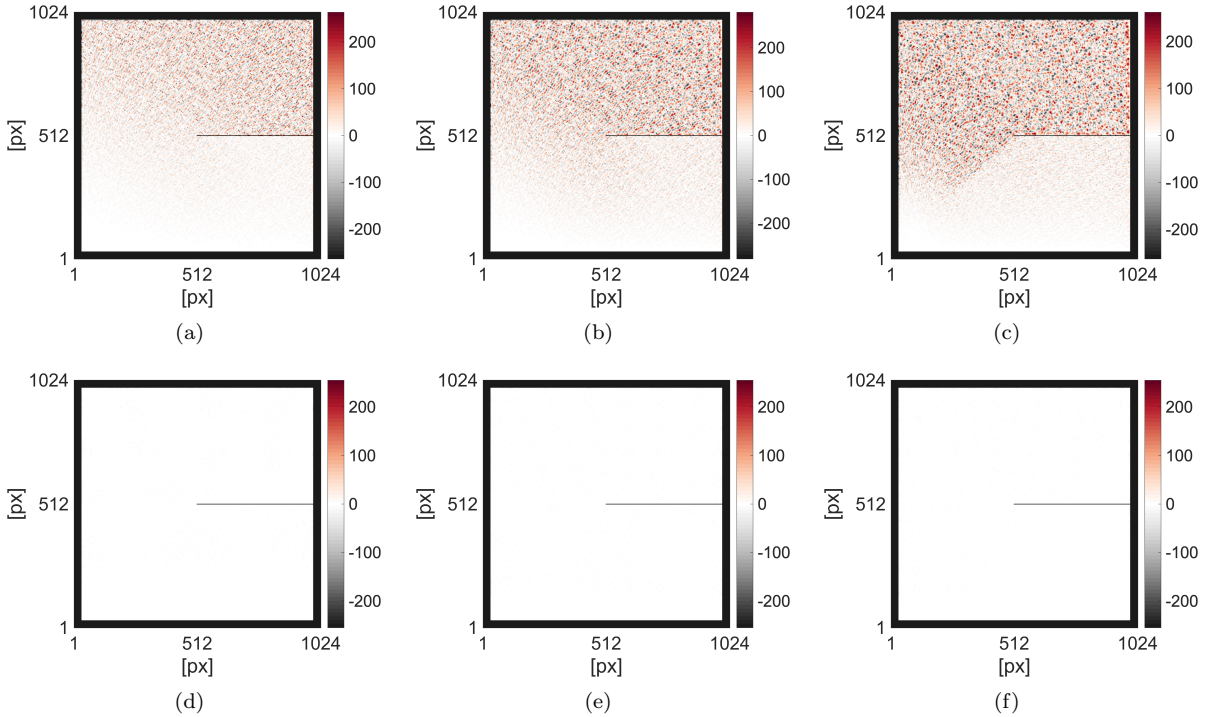

Figure 7: Initial (a-c) and converged (d-f) gray level residuals at frames 20 (a,d), 43 (b,e) and 75 (c,f) for the small-sample experiment.

By comparing the overall convergence of the residual $\|\rho\|_{L^2(\mathcal{I};\Omega)}/|\mathcal{I}\times\Omega|$ (Figure 8(a)) with the convergence

of the relative error of the parameters (Figure 8(b))

$$\mathcal{R}_i = \frac{|a_i - a_i^{\text{real}}|}{|a_i^{\text{real}}|}, \tag{39}$$

one observes that the first reduction of the residual is related to the boundary conditions. Moreover, the parameters a_1 and a_2 are, on average, the most accurate parameters. Even though the residual barely reduced after iteration 7, the parameters and the displacement field still changed quite a lot. After the fifth iteration, an exponential convergence rate was reached and after the twelfth iteration, the sum of $\|\delta a_i / a_i^{(0)}\|$ was less than 10^{-3} such that the iteration was stopped.

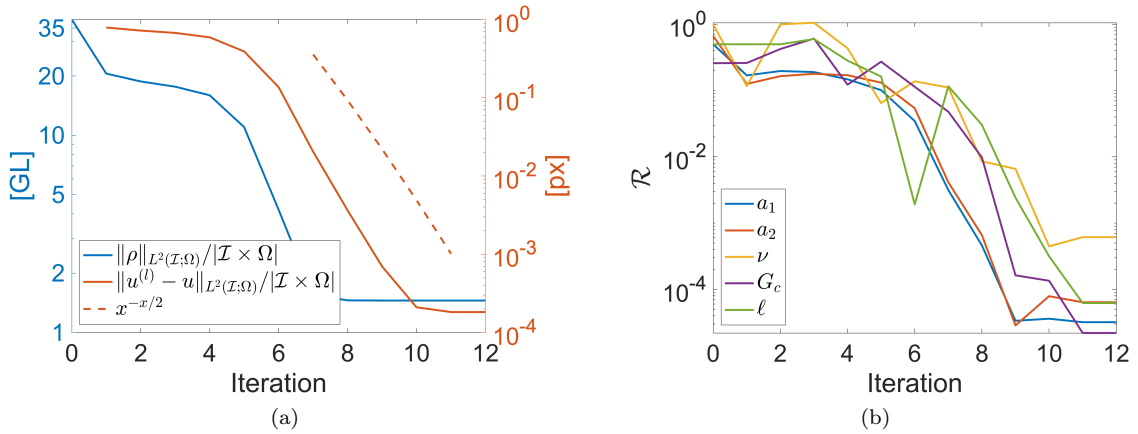

Figure 8: Small-sample experiment. Convergence of the residual $\mathcal{J}_2$ and difference of the approximate and true displacement compared to an exponential convergence rate (dashed line) (a). Convergence of the relative error $\mathcal{R}$ defined by Equation (39) for the five identified parameters (b).

4.1.3. Influence of acquisition noise

So far, the virtual images were assumed to be almost optimal i.e., they were constructed such that the gray level conservation held, except for interpolation errors. Real images include much larger errors due to acquisition noise that can be modeled by Gaussian white noise η such that the gray level conservation becomes

$$I_0(\boldsymbol{x}) = I^{\mathcal{M}(\boldsymbol{p})}(\boldsymbol{x}, t) + \eta(\boldsymbol{x}, t). \tag{40}$$

The influence of noise is analyzed by adding Gaussian white noise with different standard deviation levels to all images, while the identification scheme remains the same. In Figure 9, the relative error $\mathcal{R}_i$ for each parameter is reported for different levels of noise. Despite the fact that one would typically only expect standard deviations of about 5% of the dynamic range (at the most) i.e., 12.75 GL (Gray Levels), the performance of the identification procedure with standard deviations up to 20% of the dynamic range (51 GL) was investigated. Having also converged for the 20% level indicates that the presented algorithm is robust and remains very accurate. Noticeably, the relative error is less than 1% of the actual solution for 5% noise.

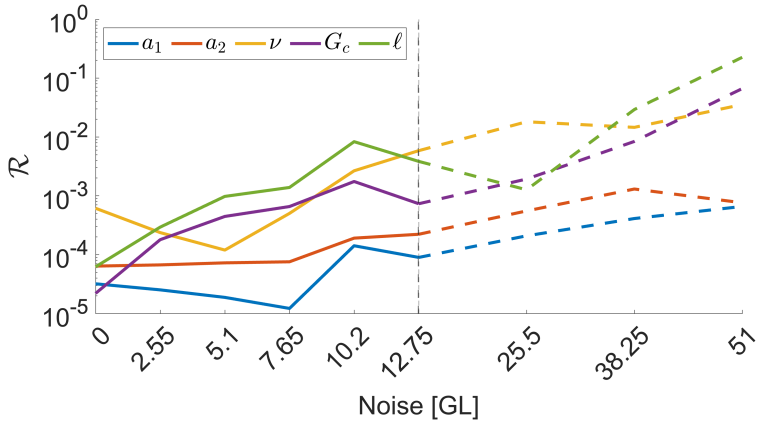

Figure 9: Convergence results for the small-sample experiment in terms of parameter errors for different levels of standard deviation of Gaussian white noise.

4.2. Large-sample experiment

The second experiment is used to analyze Algorithm 1 in a more realistic setting. Therefore, the sample is enlarged to have the same size as in the CARPIUC benchmark [11], see Figure 10(a), but the speckle pattern and the overall shape are kept the same as in the previous section, Figure 10(b). The material parameters are also adapted to be closer to a quasi-brittle material, see Table 2.

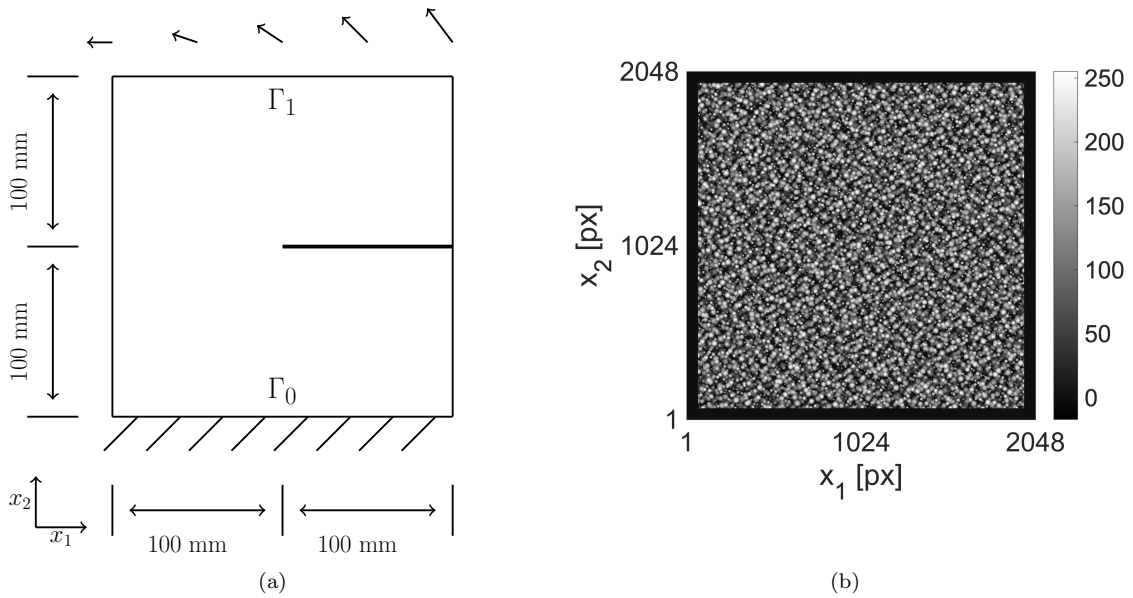

(a) (b)

Figure 10: Large-sample experiment. Geometry of the sample and applied boundary conditions (a), speckle pattern applied to the sample surface (b). The pixel size is 104 µm.

Table 2: Reference material and numerical parameters to generate the displacement fields for the deformed configurations for the large-sample experiment.

Parameter	Definition	Value
h	Diagonal cell diameter	2.4 mm (or $\approx$ 23 px)
G_c	Fracture energy	0.3 kJ/m^2
E	Young's modulus	15 GPa
ν	Poisson's ratio	0.2
ℓ	Internal length	$2\,h \approx 4.7$ mm (or $\approx$ 46 px)
κ	Regularization parameter	10^{-10}

The following boundary condition

$$\boldsymbol{u}|_{\Gamma_0} = 0 \text{ [mm]} \quad \text{and} \quad \boldsymbol{u}|_{\Gamma_1} = (-50\,\tau, 1/4\,x_1\,\tau)^T \text{ [mm]} \tag{41}$$

results in a similar crack pattern as in the first test, see Figure 11, but this time with the end time of $\tau = 7.5 \cdot 10^{-3}$ and a pixel size of about 104 µm the maximum displacement at the boundary Γ_1 is about 3.6 px. Therefore, the maximum displacement in terms of pixels is reduced by a factor of about 5 compared to the small-sample test. This level allows for a comparison of the two tests and the convergence of the algorithm.

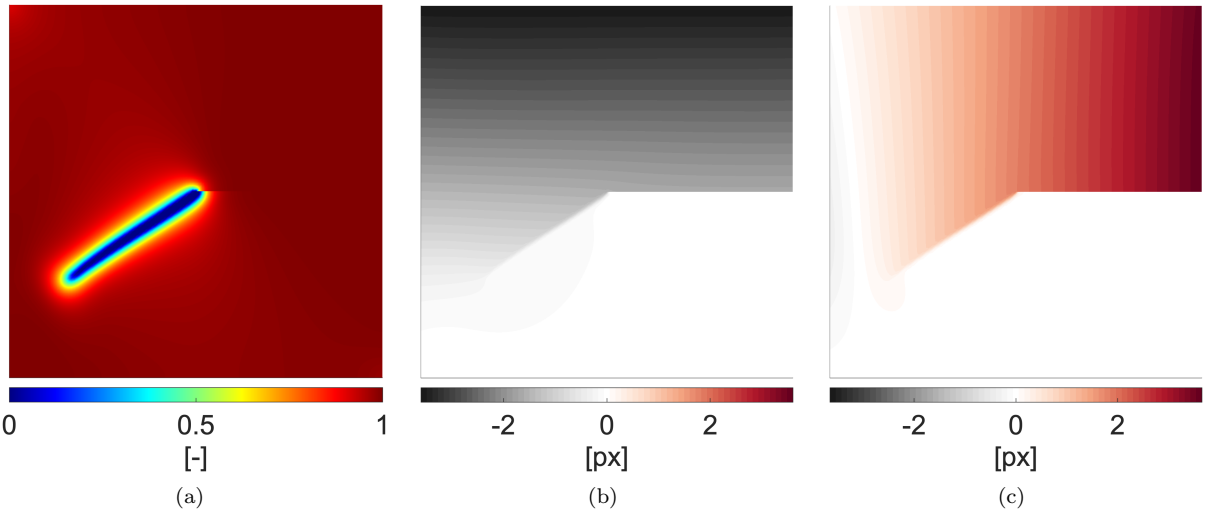

(a) (b) (c)

Figure 11: Solution of the phase-field model of the large-sample test at frame 75 for the reference parameters. Phase-field variable φ (a), displacements u_1 (b) and u_2 (c).

The parameterization $\boldsymbol{p} = (a_1, ..., a_5)^T \in \mathbb{P}$ is defined as

$$\boldsymbol{u}|_{\Gamma_1 \times \mathcal{I}} = (10a_1\, t, a_2/20\, x_1\, t)^T, \quad \nu = a_3, \quad G_c = a_4 \quad \text{and} \quad \ell = a_5\, h, \tag{42}$$

and the initial parameterization was chosen to be

$$\boldsymbol{p}^0 = (a_1^{(0)}, ..., a_5^{(0)}) = (-1, 1, 0.4, 0.5, 3)^T, \tag{43}$$

such that, similar to the first test, no crack has propagated.

4.2.1. Conditioning study

Similar to the first experiment, the full space-time Hessian matrix has a lower condition number than any instantaneous Hessian matrix as shown in Figure 12. Yet, the eigenvalues are much lower, while the eigenmodes are essentially the same.

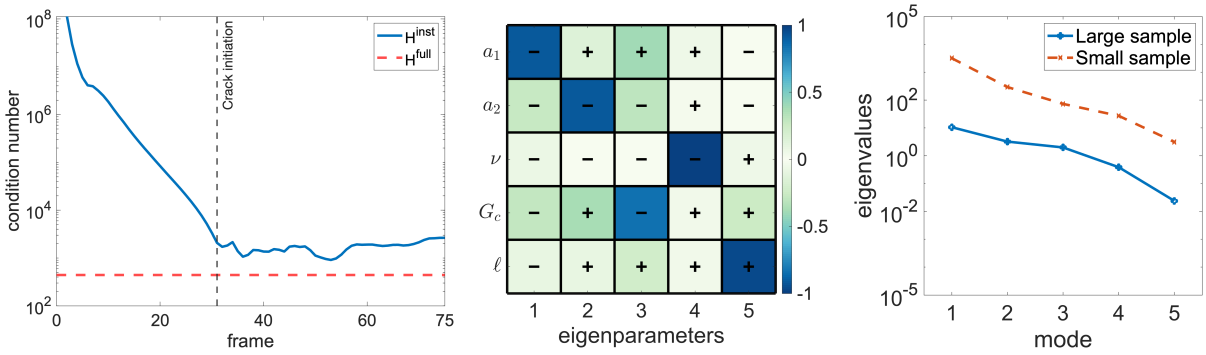

(a) (b) (c)

Figure 12: Condition number of the space-time Hessian matrix H^{full} compared to that of the instantaneous Hessian matrix H^{inst} for each image of the large-sample experiment (a), the eigenparameters of the space-time Hessian (b) and its eigenvalues (c).

4.2.2. Influence of noise

Gaussian white noise was added up to 20% of the dynamic range. One can see in Figure 13 that the error increased by a factor of about 100 between 1% (0.5 GL) to 3% (1.5 GL) noise. Nevertheless, today's cameras are able to acquire images with noise levels of about 1% of the dynamic range, such that also the internal length is expected to be measurable in real-world settings. Furthermore, the error remained relatively stable even for high noise levels. Thus, the low eigenvalues lead to robustness with respect to Gaussian noise.

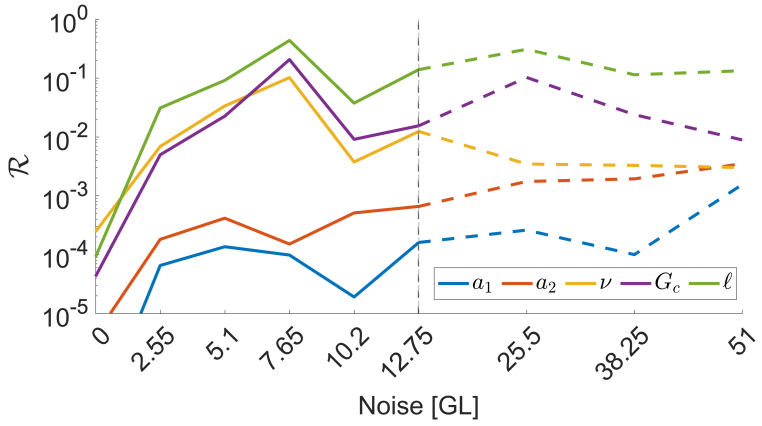

Figure 13: Convergence results for the large-sample experiment in terms of parameter errors for different levels of standard deviation of Gaussian white noise.

5. Conclusion and Outlook

In this study, a phase-field fracture model was included into an integrated-DIC framework, enabling for the identification of material parameters and boundary conditions. In the first parts of this work, algorithms and conceptional developments were designed in order to utilize numerically a modern phase-field fracture approach with primal-dual active set techniques and parallel computing. Phase-field fracture acted as inner approach of IDIC. Two synthetic experiments were designed based on realistic sample geometries, boundary conditions, image contrast and acquisition noise. The samples were deformed with the phase-field model with realistic material parameters until a crack initiated and propagated.

The results showed the capability to simultaneously identify the boundary conditions and material parameters for the whole acquisition of a single experiment. For both experiments, the parameter sensitivity fields, their relative coupling and amplitudes were investigated at different crack propagation steps. Remarkably, high sensitivities were obtained for Poisson's ratio and the internal length through the proposed space-time formulation for the first test case (*i.e.*, the influence of acquisition noise on the calibration results remained limited over a very large range of standard deviations). The identification of those two parameters is frequently highlighted as challenging in the literature. For the second test case, which was more challenging in terms of noise to signal ratio, good calibration results were obtained for a more limited range of acquisition noise. Such observations show that the sensitivity analyses as discussed herein are very useful to probe IDIC frameworks prior to actual experiments.

Since the present analysis effectively demonstrated the potential for coupling the phase-field fracture model with IDIC using synthetic test cases, a future study is to apply it to real experiments (*e.g.*, the so-called CARPIUC benchmark [11]), from which the synthetic experiments were inspired. Using projection-based digital volume correlation (P-DVC), it would also be possible to extend the analysis to 4D measurements [39, 46]. Additionally, even though the presented method converged fast, it may be interesting to further investigate the computation of the sensitivities for each parameter. This step requires a full computation of the phase-field model for each parameter at each Newton iteration, which is in the end a costly operation.

Acknowledgments

The financial support of the French-German University through the French-German Doctoral college "Sophisticated Numerical and Testing Approaches" (CDFA-DFDK 19-04) is acknowledged. Discussions are acknowledged within the framework of the International Research Training Group on Computational Mechanics Techniques in High Dimensions GRK 2657 funded by the German Research Foundation (DFG) under Grant Number 433082294.

References

[1] M. Ambati, T. Gerasimov, and L. De Lorenzis. A review on phase-field models of brittle fracture and a new fast hybrid formulation. *Computational Mechanics*, 55(2):383–405, 2015.

[2] D. Arndt, W. Bangerth, D. Davydov, T. Heister, L. Heltai, M. Kronbichler, M. Maier, J.-P. Pelteret, B. Turcksin, and D. Wells. The deal.ii finite element library: Design, features, and insights. *Computers & Mathematics with Applications*, 2020.

[3] D. Arndt, W. Bangerth, M. Feder, M. Fehling, R. Gassmöller, T. Heister, L. Heltai, M. Kronbichler, M. Maier, P. Munch, J.-P. Pelteret, S. Sticko, B. Turcksin, and D. Wells. The deal.ii library, version 9.4. *Journal of Numerical Mathematics*, 30(3):231–246, 2022.

[4] I. Babuska and U. Banerjee. Stable Generalized Finite Element Method (SGFEM). *Computer Methods in Applied Mechanics and Engineering*, 201-204(0):91 – 111, 2012.

[5] Z. P. Bažant and G. Pijaudier-Cabot. Measurement of characteristic length of nonlocal continuum. *Journal of Engineering Mechanics*, 115(4):755–767, 1989.

[6] G. Besnard, H. Leclerc, S. Roux, and F. Hild. Analysis of image series through digital image correlation. *J. Strain Analysis*, 47(4):214–228, 2012.

[7] B. Bourdin, G. Francfort, and J.-J. Marigo. Numerical experiments in revisited brittle fracture. *Journal of the Mechanics and Physics of Solids*, 48(4):797–826, 2000.

[8] B. Bourdin, G. Francfort, and J.-J. Marigo. The variational approach to fracture. *J. Elasticity*, 91(1–3):1–148, 2008.

[9] B. Bourdin and G. A. Francfort. Past and present of variational fracture. *SIAM News*, 52(9), 2019.

[10] C. Burstedde, L. C. Wilcox, and O. Ghattas. P4est: Scalable algorithms for parallel adaptive mesh refinement on forests of octrees. *SIAM J. Sci. Comput.*, 33(3):1103–1133, May 2011.

[11] A. Carpiuc, M. Poncelet, J. Réthoré, and S. Roux. Carpiuc benchmark overview: crack advance, reorientation, propagation and initiation under complex loadings. *Advanced Modeling and Simulation in Engineering Sciences*, 5:24, 2018.

[12] A. Carpiuc-Prisacari, M. Poncelet, K. Kazymyrenko, F. Hild, and H. Leclerc. Comparison between experimental and numerical results of mixed-mode crack propagation in concrete: Influence of boundary conditions choice. *Cement and Concrete Research*, 100:329–340, 2017.

[13] C. Chang and M. E. Mear. A boundary element method for two dimensional linear elastic fracture analysis. *International Journal of Fracture*, 74:219–251, 1995.

[14] S. L. Crouch. Solution of plane elasticity problems by the displacement discontinuity method. i. infinite body solution. *International Journal for Numerical Methods in Engineering*, 10(2):301–343, 1976.

[15] R. de Borst and C. Verhoosel. Gradient damage vs phase-field approaches for fracture: Similarities and differences. *Computer Methods in Applied Mechanics and Engineering*, 312(December):78–94, 2016.

[16] J. Desai, G. Allaire, and F. Jouve. Topology optimization of structures undergoing brittle fracture. *Journal of Computational Physics*, 458:111048, 2022.

[17] R. Desmorat, F. Gatuingt, and M. Jirásek. Nonlocal models with damage-dependent interactions motivated by internal time. *Engineering Fracture Mechanics*, 142:255–275, 2015.

[18] P. Diehl, R. Lipton, T. Wick, and M. Tyagi. A comparative review of peridynamics and phase-field models for engineering fracture mechanics. *Computational Mechanics*, 69:1259–1293, 2022.

[19] J. Donnini, G. Lancioni, G. Chiappini, and V. Corinaldesi. Uniaxial tensile behavior of ultra-high performance fiber-reinforced concrete (uhpfrc): Experiments and modeling. *Composite Structures*, 258:113433, 2021.

[20] R. Fedele, L. Galantucci, and A. Ciani. Global 2d digital image correlation for motion estimation in a finite element framework: a variational formulation and a regularized, pyramidal, multi-grid implementation. *International Journal for Numerical Methods in Engineering*, 96, 12 2013.

[21] G. Francfort and J.-J. Marigo. Revisiting brittle fracture as an energy minimization problem. *Journal of the Mechanics and Physics of Solids*, 46(8):1319–1342, 1998.

[22] T.-P. Fries and T. Belytschko. The extended/generalized finite element method: An overview of the method and its applications. *Int. J. Numer. Meth. Engrg.*, 84:253–304, 2010.

[23] M. Geers, R. De Borst, and T. Peijs. Mixed numerical-experimental identification of non-local characteristics of random-fibre-reinforced composites. *Compos. Sci. Tech.*, 59:1569–1578, 1999.

[24] T. Gerasimov, U. Römer, J. Vondřejc, H. G. Matthies, and L. De Lorenzis. Stochastic phase-field modeling of brittle fracture: Computing multiple crack patterns and their probabilities. *Computer Methods in Applied Mechanics and Engineering*, 372:113353, 2020.

[25] M. Grédiac and F. Hild, editors. *Full-Field Measurements and Identification in Solid Mechanics*. ISTE / Wiley, London (UK), 2012.

[26] I. Grešovnik. Ageneral purpose computational shell for solving inverse and optimisation problems. *University of Wales*, 2000.

[27] A. C. Hansen-Dörr, L. Wilkens, A. Croy, A. Dianat, G. Cuniberti, and M. Kästner. Combined molecular dynamics and phase-field modelling of crack propagation in defective graphene. *Computational Materials Science*, 163:117–126, 2019.

[28] T. Heister, M. F. Wheeler, and T. Wick. A primal-dual active set method and predictor-corrector mesh adaptivity for computing fracture propagation using a phase-field approach. *Computer Methods in Applied Mechanics and Engineering*, 290:466–495, 2015.

[29] T. Heister and T. Wick. Parallel solution, adaptivity, computational convergence, and open-source code of 2d and 3d pressurized phase-field fracture problems. *PAMM*, 18(1):e201800353, 2018.

[30] T. Heister and T. Wick. pfm-cracks: A parallel-adaptive framework for phase-field fracture propagation. *Software Impacts*, 6:100045, 2020.

[31] M. A. Heroux, R. A. Bartlett, V. E. Howle, R. J. Hoekstra, J. J. Hu, T. G. Kolda, R. B. Lehoucq, K. R. Long, R. P. Pawlowski, E. T. Phipps, A. G. Salinger, H. K. Thornquist, R. S. Tuminaro, J. M. Willenbring, A. Williams, and K. S. Stanley. An overview of the trilinos project. *ACM Trans. Math. Softw.*, 31(3):397–423, 2005.

[32] N. J. Higham. *Accuracy and Stability of Numerical Algorithms*. Society for Industrial and Applied Mathematics, USA, 2nd edition, 2002.

[33] F. Hild, A. Bouterf, L. Chamoin, F. Mathieu, J. Neggers, F. Pled, Z. Tomičević, and S. Roux. Toward 4d mechanical correlation. *Adv. Mech. Simul. Eng. Sci.*, 3(1):1–26, 2016.

[34] F. Hild and S. Roux. Digital image correlation: From measurement to identification of elastic properties - a review. *Strain*, 42:69–80, 2006.

[35] F. Hild and S. Roux. Digital image correlation. In P. Rastogi and E. Hack, editors, *Optical Methods for Solid Mechanics. A Full-Field Approach*, pages 183–228, Weinheim (Germany), 2012. Wiley-VCH.

[36] L. Hug, G. Dahan, S. Kollmannsberger, E. Rank, and Z. Yosibash. Predicting fracture in the proximal humerus using phase field models. *Journal of the Mechanical Behavior of Biomedical Materials*, 134:105415, 2022.

[37] D.-A. Hun, J. Yvonnet, J. Guilleminot, A. Dadda, A.-M. Tang, and M. Bornert. Desiccation cracking of heterogeneous clayey soil: Experiments, modeling and simulations. *Engineering Fracture Mechanics*, 258:108065, 2021.

[38] C. Iacono, L. Sluys, and J. van Mier. Estimation of model parameters in nonlocal damage theories by inverse analysis techniques. *Computer Methods in Applied Mechanics and Engineering*, 195(52):7211–7222, 2006. Computational Modelling of Concrete.

[39] C. Jailin, A. Buljac, A. Bouterf, F. Hild, and S. Roux. Fast four-dimensional tensile test monitored via x-ray computed tomography: Elastoplastic identification from radiographs. *The Journal of Strain Analysis for Engineering Design*, 54(1):44–53, 2019.

[40] C. Jailin, A. Carpiuc, K. Kazymyrenko, M. Poncelet, H. Leclerc, F. Hild, and S. Roux. Virtual hybrid test control of sinuous crack. *Journal of the Mechanics and Physics of Solids*, 102:239–256, 2017.

[41] D. Jodlbauer, U. Langer, and T. Wick. Matrix-free multigrid solvers for phase-field fracture problems. *Computer Methods*

in Applied Mechanics and Engineering, 372:113431, 2020.

[42] D. Khimin, M. Steinbach, and T. Wick. Space-time formulation, discretization, and computational performance studies for phase-field fracture optimal control problems. *Journal of Computational Physics*, 470:111554, 2022.

[43] D. Khimin, M. Steinbach, and T. Wick. Space-time mixed system formulation of phase-field fracture optimal control problems. *Journal of Optimization Theory and Applications*, 2023, accepted for publication.

[44] A. Khodadadian, N. Noii, M. Parvizi, M. Abbaszadeh, T. Wick, and C. Heitzinger. A bayesian estimation method for variational phase-field fracture problems. *Computational Mechanics*, 66:827–849, 2020.

[45] L. Kolditz, K. Mang, and T. Wick. A modified combined active-set newton method for solving phase-field fracture into the monolithic limit. *Computer Methods in Applied Mechanics and Engineering*, 414:116170, 2023.

[46] V. Kosin, A. Fau, C. Jailin, B. Smaniotto, T. Wick, and F. Hild. A projection-based approach to extend digital volume correlation for 4D spacetime measurements. *Comptes Rendus. Mécanique*, 351:265–280, 2023.

[47] C. Kuhn and R. Müller. A continuum phase field model for fracture. *Engineering Fracture Mechanics*, 77(18):3625 – 3634, 2010. Computational Mechanics in Fracture and Damage: A Special Issue in Honor of Prof. Gross.

[48] A. Kumar, B. Bourdin, G. A. Francfort, and O. Lopez-Pamies. Revisiting nucleation in the phase-field approach to brittle fracture. *Journal of the Mechanics and Physics of Solids*, 142:104027, 2020.

[49] C. Le Bellégo, J. F. Dubé, G. Pijaudier-Cabot, and B. Gérard. Calibration of nonlocal damage model from size effect tests. *European Journal of Mechanics - A/Solids*, 22(1):33–46, 2003.

[50] H. Leclerc, J. Neggers, F. Mathieu, F. Hild, and S. Roux. *Correli 3.0*. IDDN.FR.001.520008.000.S.P.2015.000.31500, Agence pour la Protection des Programmes, Paris (France), 2015.

[51] H. Leclerc, J. Périé, S. Roux, and F. Hild. *Integrated digital image correlation for the identification of mechanical properties*, volume LNCS 5496, pages 161–171. Springer, Berlin (Germany), 2009.

[52] J. Lemaitre. *A Course on Damage Mechanics*. Springer Berlin, Heidelberg, 1996.

[53] J. Lemaitre and J.-L. Chaboche. Mechanics of solid materials. *Cambridge university press*, 1994.

[54] J. Lemaitre and R. Desmorat. *Engineering damage mechanics: ductile, creep, fatigue and brittle failures*. Springer, 2005.

[55] J. Lemaitre and J. Dufailly. Damage measurements. *Eng. Fract. Mech.*, 28(5-6):643–661, 1987.

[56] D. Lindner, F. Mathieu, F. Hild, O. Allix, C. Ha Minh, and O. Paulien-Camy. On the evaluation of stress triaxiality fields in a notched titanium alloy sample via integrated DIC. *J. Appl. Mech.*, 82(7):071014, 2015.

[57] F. Mathieu, H. Leclerc, F. Hild, and S. Roux. Estimation of elastoplastic parameters via weighted FEMU and integrated-DIC. *Exp. Mech.*, 55(1):105–119, 2015.

[58] C. Miehe, M. Hofacker, and F. Welschinger. A phase field model for rate-independent crack propagation: Robust algorithmic implementation based on operator splits. *Computer Methods in Applied Mechanics and Engineering*, 199(45):2765–2778, 2010.

[59] C. Miehe, F. Welschinger, and M. Hofacker. Thermodynamically consistent phase-field models of fracture: Variational

principles and multi-field FE implementations. *International Journal for Numerical Methods in Engineering*, 83(10):1273–1311, 2010.

[60] N. Moës, J. Dolbow, and T. Belytschko. A finite element method for crack growth without remeshing. *Int. J. Num. Meth. Eng.*, 46(1):133–150, 1999.

[61] M. Mohammadi and W. Wollner. A priori error estimates for a linearized fracture control problem. *Optimization and Engineering*, 22:2127–2149, 2021.

[62] S. Na, W. Sun, M. D. Ingraham, and H. Yoon. Effects of spatial heterogeneity and material anisotropy on the fracture pattern and macroscopic effective toughness of mancos shale in brazilian tests. *Journal of Geophysical Research: Solid Earth*, 122(8):6202–6230, 2017.

[63] J. Neggers, J. Hoefnagels, M. Geers, F. Hild, and S. Roux. Time-resolved integrated digital image correlation. *Int. J. Num. Meth. Eng.*, 203(3):157–182, 2015.

[64] I. Neitzel, T. Wick, and W. Wollner. An optimal control problem governed by a regularized phase-field fracture propagation model. *SIAM Journal on Control and Optimization*, 55(4):2271–2288, 2017.

[65] I. Neitzel, T. Wick, and W. Wollner. An optimal control problem governed by a regularized phase-field fracture propagation model. part II: The regularization limit. *SIAM Journal on Control and Optimization*, 57(3):1672–1690, 2019.

[66] T. Nguyen, J. Yvonnet, M. Bornert, and C. Chateau. Initiation and propagation of complex 3d networks of cracks in heterogeneous quasi-brittle materials: Direct comparison between in situ testing-microct experiments and phase field simulations. *Journal of the Mechanics and Physics of Solids*, 95:320–350, 2016.

[67] T. Nguyen, J. Yvonnet, Q.-Z. Zhu, M. Bornert, and C. Chateau. A phase field method to simulate crack nucleation and propagation in strongly heterogeneous materials from direct imaging of their microstructure. *Engineering Fracture Mechanics*, 139:18–39, 2015.

[68] J. Nocedal and S. Wright. *Numerical optimization*, pages 1–664. Springer Series in Operations Research and Financial Engineering. Springer Nature, 2006.

[69] N. Noii, A. Khodadadian, J. Ulloa, F. Aldakheel, T. Wick, S. Francois, and P. Wriggers. Bayesian inversion for unified ductile phase-field fracture. *Computational Mechanics*, 68:943–980, 2021.

[70] N. Noii, A. Khodadadian, and T. Wick. Bayesian inversion for anisotropic hydraulic phase-field fracture. *Computer Methods in Applied Mechanics and Engineering*, 386:114118, 2021.

[71] S. P. Patil, Y. Heider, C. A. Hernandez Padilla, E. R. Cruz-Chú, and B. Markert. A comparative molecular dynamics-phase-field modeling approach to brittle fracture. *Computer Methods in Applied Mechanics and Engineering*, 312:117–129, 2016. Phase Field Approaches to Fracture.

[72] G. Pijaudier-Cabot and Z. P. Bažant. Nonlocal damage theory. *Journal of engineering mechanics*, 113(10):1512–1533, 1987.

[73] S. I. Repin and S. Sauter. *Accuracy of mathematical models : dimension reduction, homogenization, and simplification*,

volume 33 of *EMS tracts in mathematics, 33*. European Mathematical Society;, Berlin.

[74] J. Réthoré, F. Hild, and S. Roux. Shear-band capturing using a multiscale extended digital image correlation technique. *Computer Methods in Applied Mechanics and Engineering*, 196(49):5016–5030, 2007.

[75] Y. Saad and M. H. Schultz. GMRES: A generalized minimal residual algorithm for solving nonsymmetric linear systems. *SIAM J. Sci. Stat. Comput.*, 7(3), 1986.

[76] S. A. Silling. Reformulation of elasticity theory for discontinuities and long-range forces. *Journal of the Mechanics and Physics of Solids*, 48(1):175–209, 2000.

[77] R. C. Smith. *Uncertainty Quantification: Theory, Implementation, and Applications*. SIAM, 2014.

[78] M. Sutton. Computer vision-based, noncontacting deformation measurements in mechanics: A generational transformation. *Appl. Mech. Rev.*, 65(AMR-13-1009):050802, 2013.

[79] M. Sutton, J. Orteu, and H. Schreier. *Image correlation for shape, motion and deformation measurements: Basic Concepts, Theory and Applications*. Springer, New York, NY (USA), 2009.

[80] E. Tanné, T. Li, B. Bourdin, J.-J. Marigo, and C. Maurini. Crack nucleation in variational phase-field models of brittle fracture. *J. Mech. Phys. Solids*, 110:80–99, 2018.

[81] A. Tsitova, F. Bernachy-Barbe, B. Bary, C. Bourcier, and F. Hild. Identification of microscale fracture models for mortar with in-situ tests. *International Journal of Mechanical Sciences*, 242:107988, 2023.

[82] T. Wick. *Multiphysics Phase-Field Fracture: Modeling, Adaptive Discretizations, and Solvers*. De Gruyter, Berlin, Boston, 2020.

[83] J.-Y. Wu, V. P. Nguyen, C. Thanh Nguyen, D. Sutula, S. Bordas, and S. Sinaie. Phase field modelling of fracture. *Advances in Applied Mechanics*, 53:1–183, 09 2019.

[84] T. Wu, A. Carpiuc-Prisacari, M. Poncelet, and L. De Lorenzis. Phase-field simulation of interactive mixed-mode fracture tests on cement mortar with full-field displacement boundary conditions. *Engineering Fracture Mechanics*, 182:658–688, 2017.

[85] T. Wu, B. Rosic, L. de Lorenzis, and H. Matthies. Parameter identification for phase-field modeling of fracture: a Bayesian approach with sampling-free update. *Computational Mechanics*, 67:435–453, 2021.

[86] D. Xenos, D. Grégoire, S. Morel, and P. Grassl. Calibration of nonlocal models for tensile fracture in quasi-brittle heterogeneous materials. *Journal of the Mechanics and Physics of Solids*, 82:48–60, 2015.

[87] B. Xu, T. Xu, Y. Xue, M. Heap, P. Ranjith, P. Wasantha, and Z. Li. Phase-field modeling of crack growth and interaction in rock. *Geomechanics and Geophysics for Geo-Energy and Geo-Resources*, 8:180, 2022.

[88] X. P. Xu and A. Needleman. Numerical simulations of fast crack growth in brittle solids. *J. Mech. Phys. Solids*, 42:1397–1434, 1994.